Carbon Nanospheres Loaded with Ir Single Atoms: Enhancing the Activity toward Formic Acid Oxidation by Increasing the Porosity

Jacob Jeskey,[a] Yong Ding,[b] Yidan Chen,[b] Zachary D. Hood,[c] Hongliang Li,[d] George E. Sterbinsky,[e] and Younan Xia[a,f]*

[a]School of Chemistry and Biochemistry, Georgia Institute of Technology, Atlanta, Georgia 30332, United States

[b]School of Materials Science and Engineering, Georgia Institute of Technology, Atlanta, Georgia 30332, United States

[c]Applied Materials Division, Argonne National Laboratory, Lemont, Illinois 60439, United States

[d]Hefei National Research Center for Physical Sciences at the Microscale, University of Science and Technology of China, Hefei, Anhui 230026, PR China

[e]Advanced Photon Source, Argonne National Laboratory, Lemont, Illinois 60439, United States

[f]The Wallace H. Coulter Department of Biomedical Engineering, Georgia Institute of Technology and Emory University, Atlanta, Georgia 30332, United States

*Corresponding author: younan.xia@bme.gatech.edu

Abstract: Theoretically, single-atom catalysts (SACs) offer 100% atom utilization, making them strong candidates to replace expensive nanoparticles for catalysis. However, the structural supports used to anchor the SACs dramatically reduce the utilization efficiency of atoms (*i.e.*, the percent of atoms actually accessible by reactants) by either encapsulating the SACs completely or creating severe diffusion limitation. Either of which leads to an overall low atom utilization and thus poor electrocatalytic activity similar to that of nanoparticles. In addressing this issue, we systematically investigated how the porous structure of carbon nanospheres affects the activity of Ir-SACs toward formic acid oxidation (FAO). Specifically, we utilized a kinetically-controlled growth strategy to produce Ir-SACs loaded in uniform carbon nanospheres featuring yolk-shell, mesoporous, and hollow structures. At a high specific surface area of 441 m^2 g^{-1} and exposed metal content of 1.82 wt.%, the Ir-SACs based on mesoporous carbon nanospheres showed a remarkable FAO peak current density of 30.6 mA cm^{-2}, which was 283 and 46 times greater when benchmarked against the catalysts based on solid carbon nanospheres and 20 wt.% Ir/C, respectively.

Introduction

Single-atom catalysts (SACs) have recently emerged as one of the most active research areas in catalysis.[1-3] The theoretical 100% atom utilization and remarkable selectivity make SACs an ideal candidate to replace conventional metal nanoparticles.[4,5] However, their production methods are still inadequate for large scale industrial applications.[6,7] In the context of electrocatalysis, two synthetic strategies are commonly used to produce SACs on carbon supports, including the post-modification, incipient wetness impregnation (IWI) technique where metal ions are adsorbed and then reduced on pre-fabricated supports, and the in-situ (or pyrolysis) method where the SACs and support are formed at the same time. The IWI technique produces SACs on the surface of a carbon substrate and essentially all of the metal atoms are accessible for catalysis, albeit high loadings are challenging owing to the formation of nanoparticles. As such, the IWI technique is only suitable for fundamental studies, not viable for industrial applications because of the low metal content and tedious multi-step process.[8,9] On the other hand, the in-situ method involves a simple one-pot synthesis and can produce SACs at a much higher loading. Unfortunately, the majority of the SACs will be trapped within the carbon matrix, resulting in poor performance due to the impeded diffusion of reactant and product molecules during catalysis.[9] In a recent study, we demonstrated the use of chemical confinement to produce transition metal SACs on uniform solid carbon nanospheres through a one-pot approach.[10] The uniform size of the carbon nanospheres can help mitigate the diffusion limitation as the ordered, close-packing array contains interspatial channels to facilitate the transportation of molecular species. However, this feature only benefits the SACs located on the surface of a nanosphere; those inside the nanosphere are still inaccessible.[11-13] To address the accessibility issue, this work aims to improve the accessibility of internal SACs by introducing mesoporous, yolk-shell, and hollow structures into the carbon nanospheres.

To our knowledge, the aforementioned structural features have yet to be achieved with SACs without the use of template-directed or post-modification methods. It would be of great interest to develop a simple, versatile, and cost-effective method for the synthesis of SACs in hollow/porous carbon nanospheres. Recently, there has been significant innovation in the synthesis of carbon nanospheres from a phenolic resin precursor, where hollow/porous attributes were made possible using a template- and surfactant-free process. Briefly, during the initial polymerization of 3-aminophenol and formaldehyde, monomers quickly react to form droplets comprised of small

phenolic oligomers. Thereafter, crosslinking occurs to harden the droplets into solid polymer nanospheres.[10,13] To this end, Bin and coworkers demonstrated that the crosslinking process actually began from the outer surface of the droplet owing to its direct exposure to the reaction solution.[14] Under normal conditions, this outside-in hardening occurs rapidly and often goes unnoticed. However, if the reaction conditions are tuned to favor slow crosslinking kinetics, then it is possible to produce a structure where the droplet surface is comprised of crosslinked network polymers while the interior remains as soluble oligomers. This inhomogeneity can be exploited by dissolving the interior with an organic solvent to produce hollow polymer nanospheres. Significantly, further tuning the reaction conditions can present mesoporous, yolk-shell, and even multi-shelled structures.[14-16] In principle, it would be practical to adopt these synthetic strategies to increase the accessibility of SACs while maintaining simplicity and cost-effectiveness. Herein we report the adoption of these strategies for the preparation of Ir-SACs with high loadings up to 1.82 wt.% and further investigate the structure-activity relationship.

Results and Discussion

In our previous work, we established a chemical confinement strategy that employes EDTA as a molecular barrier to spatially isolate transition metal atoms from each other.[10] Building upon this work, here we demonstrate that EDTA can also be used to prepare SACs with noble-metal atoms both on the surface and in the interior of uniform carbon nanospheres. Specifically, single atoms of Ir are obtained using our previous method except that Ir-EDTA is used (Figure 1). During the initial stage, 3-aminophenol and formaldehyde polymerize to produce droplets that then uptake Ir-EDTA through hydrogen bonding and ionic interactions. Meanwhile, the oligomers inside the droplets are continuously crosslinked from the outside-in, generating solid polymer nanospheres with Ir-EDTA trapped throughout the particle. Although this method can be used to achieve significant SAC loadings, the majority of the Ir atoms are trapped in the carbon matrix and thus inaccessible by the reactants. In addressing this issue, we explore several architectures to increase SAC exposure and thus enhance mass activity. As aforementioned, Bin and coworkers have previously demonstrated a kinetically-controlled synthesis to prepare yolk-shell, mesoporous, and hollow carbon nanospheres.[14] Though their report has largely inspired this work, we could only replicate their findings on small scale and had difficulty producing the desired architectures when

Ir-EDTA was introduced. Therefore, we had to modify the protocol to produce Ir-SACs hosted in yolk-shell, mesoporous, and hollow carbon nanospheres.

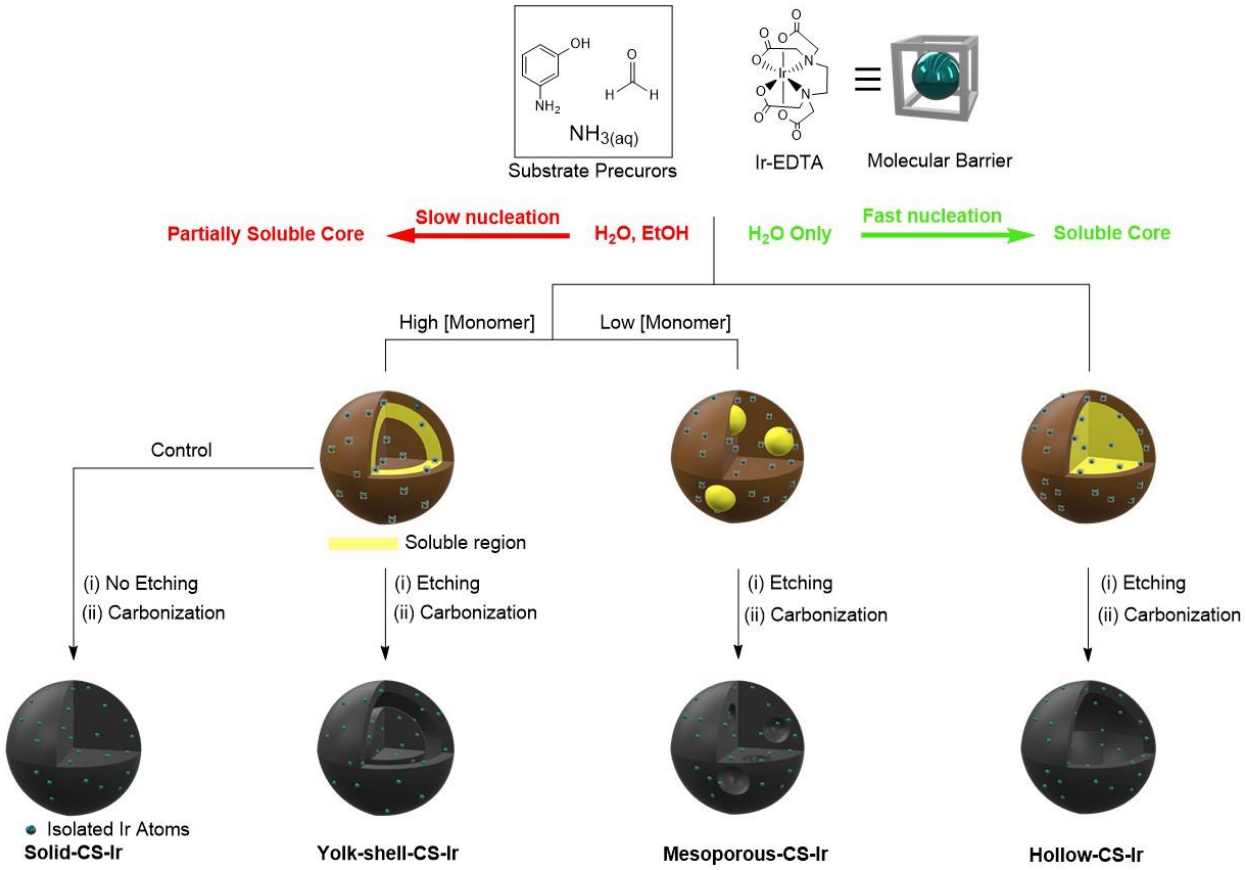

Figure 1. Schematic showing the synthesis of polymer nanospheres and then carbon nanospheres with different structures by controlling the experimental conditions. With the help of EDTA, Ir single atoms can be loaded in the carbon matrix at loading as high as 1.82 wt.% without forming nanoparticles.

As illustrated in Figure 1 and Table S1, we could change the reaction conditions to alter the polymerization kinetics and thus the structures of the resultant polymer nanospheres. The exact mechanism is yet to be fully understood and here we only offer a brief discussion of the general process. In the case of Yolk-shell-CS-Ir, the initial starting solution is composed of ethanol and water, which favors slow nucleation as ethanol can suspend the pre-polymers longer before they are phase-separated as droplets. Once the droplets are formed, the oligomers located near the water-droplet interface can quickly grow into highly-crosslinked network polymers since they are exposed to the catalyst and residual monomers in the solution. Meanwhile, the interior region has

slower polymerization kinetics due to the limited accessibility to the reaction medium, thus creating inhomogeneity within the particle. However, some of the larger interior oligomers may still be able to grow into insoluble polymers before the etching step occurs. Hence, after the particles are collected and etched with pure ethanol, a yolk-shell structure is formed. For Mesoporous-CS-Ir, by reducing the monomer concentration, we can prevent the large oligomers from forming a yolk in the core. Instead, we produce a lightly-crosslinked interior that has soluble domains throughout the core, which leads to a mesoporous structure after etching with ethanol. Lastly, for Hollow-CS-Ir, the reaction medium is changed to water only which favors extremely fast phase-separation due to the strong hydrophobic interactions among the newly-formed oligomers when suspended in an aqueous environment.[14,17,18] Due to the fast precipitation, the degree of polymerization for the interior region is significantly lower than those of the yolk-shell and mesoporous sample, thus the entire core region can be easily removed using ethanol to obtain hollow particles. Obviously, any of the routes described above can produce completely solid structures if the ethanol etching step is skipped. However, in an effort to maintain simplicity, solid particles were only produced using the protocol for the yolk-shell sample without ethanol etching.

Figure 2 shows SEM images of the Ir-loaded carbon nanospheres with different structural features obtained by controlling the experimental conditions. The solid sample appears to have a smooth outer surface consistent with our previous studies, whereas the yolk-shell sample has some visible roughness.[10,13] A large portion of the outer shells for the yolk-shell sample have also been damaged which may be a consequence of either swelling or sonication during the etching process.[19] Interestingly, worm-like channels can be observed in some of the mesoporous particles, indicating complex, interconnected pores. Lastly, some of the hollow particles have partially deflated into a concave-hollow structure which is commonly reported when the interior region is removed.[17,18] This so-called deflated-basketball structure results from a deflation-inflation process, where the solvent induces structural collapse to the polymer nanosphere during the dissolution of the interior oligomers. Thereafter, the solvent re-enters the cavity driven by osmotic pressure causing reinflation.

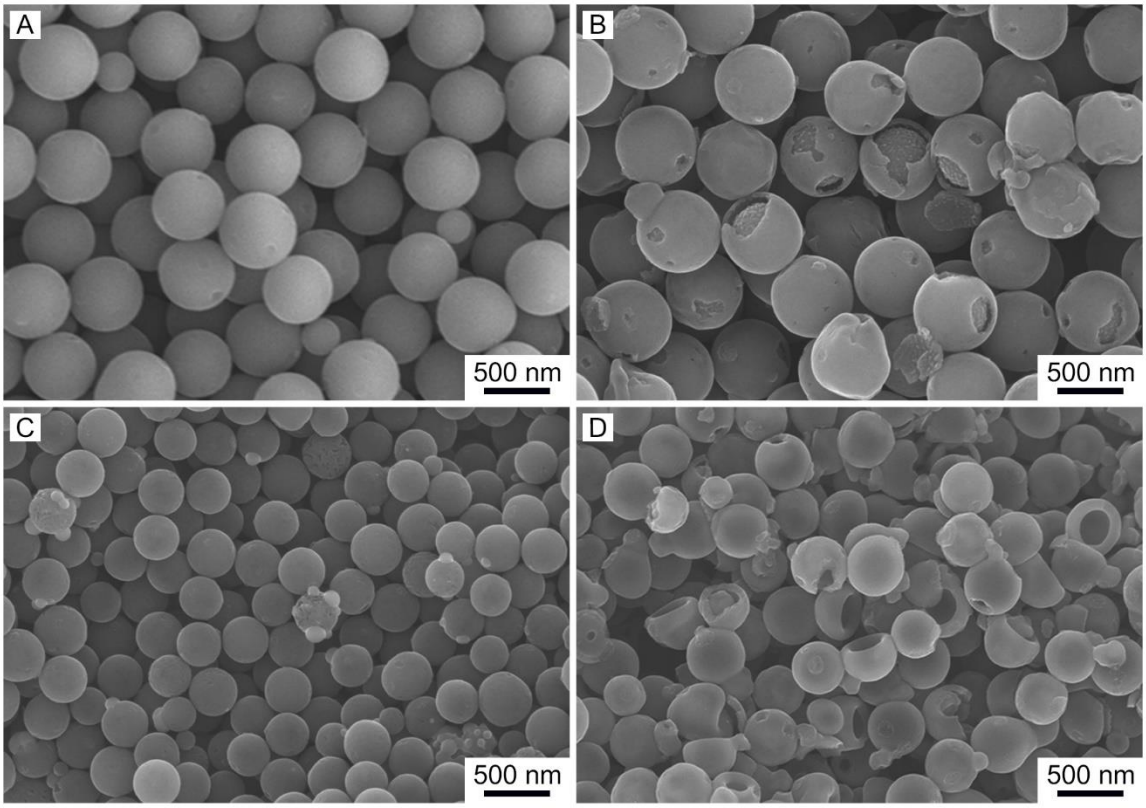

Figure 2. SEM images of (A) Solid-CS-Ir, (B) York-shell-CS-Ir, (C) Mesoporous-CS-Ir, and (D) Hollow-CS-Ir.

The HAADF-STEM images in Figures 3A and S1-3 further elucidate the structure of the carbon nanospheres and the corresponding elemental mapping shows Ir SACs uniformly dispersed throughout each particle. Specifically, Mesoporous-CS-Ir has impressive porosity in the entire particle, meaning the worm-like channels observed in the SEM images tunnel throughout the entire structure (Figure 3A). Solid-CS-Ir has no visible porosity (Figure S1), whereas Yolk-shell-CS-Ir appears to have some porosity in the core region (Figure S2). Hollow-CS-Ir has a single, large cavity in the center of particle (Figure S3). The average particle diameter and interior structural dimensions for each sample are summarized in Table S2. The atomic resolution HAADF-STEM image in Figure 2B confirms the existence of Ir exclusively as individual atoms.

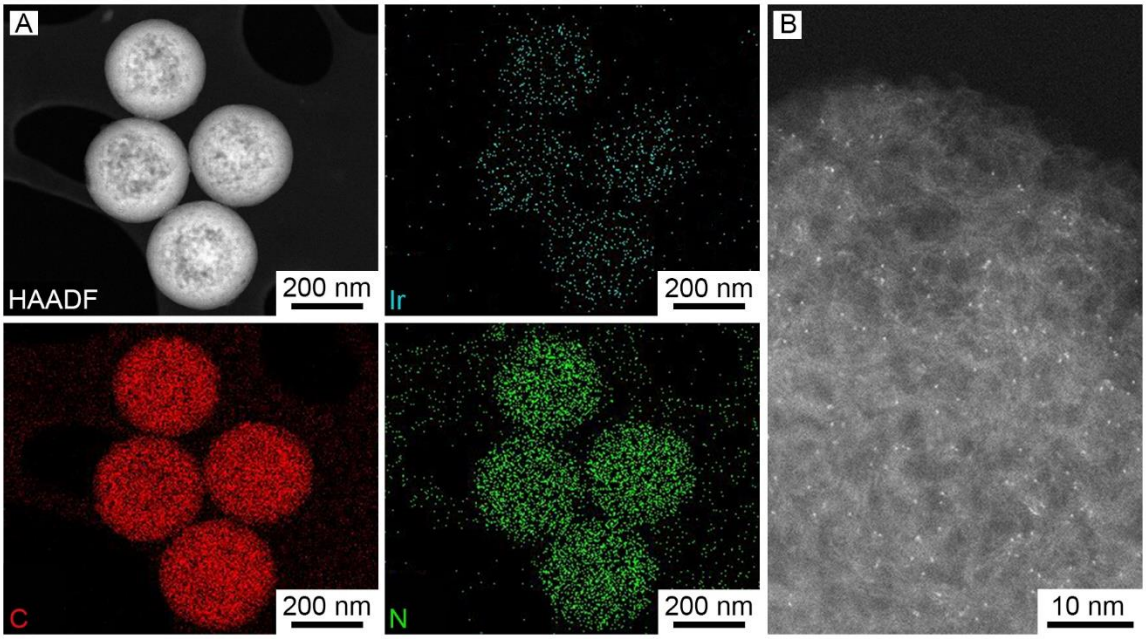

Figure 3. (A) HAADF-STEM and corresponding elemental mapping of Mesoporous-CS-Ir. (B) Atomic resolution HAADF-STEM of Mesoporous-CS-Ir sample, showing the uniform distribution of individual Ir atoms.

To further investigate the porosity, nitrogen adsorption analysis was conducted on all samples (Figure 4). The specific surface areas for Solid-CS-Ir, Yolk-shell-CS-Ir, Mesoporous-CS-Ir, and Hollow-CS-Ir were 4, 27, 441, and 251 m^2 g^{-1}, respectively (Table S3). The Solid-CS-Ir samples had a Type II isotherm indicative of a non-porous surface. Similar results were obtained for Yolk-shell-CS-Ir, except the micropore volume was slightly increased. Mesoporous-CS-Ir exhibited a Type IV isotherm with significant uptake at low pressure (below 0.2 P/P_0), indicating a mesoporous-microporous structure. The H2 hysteresis loop had delayed desorption indicative of bottle-neck pores, where constricted pore-openings prevent the condensed N_2 from evaporating until a non-equilibrium pressure is reached. However, once this pressure is reached, there is a steep desorption region indicating a narrow mesopore pore size distribution. Hollow-CS-Ir also exhibited a Type IV isotherm, however the N_2 uptake at low pressure was lower than that of mesoporous-CS-Ir, indicating a reduced microporosity. Hollow-CS-Ir showed an open ended H4 hysteresis, indicating a diffusion limited slit-pore shape caused by graphitic layers.

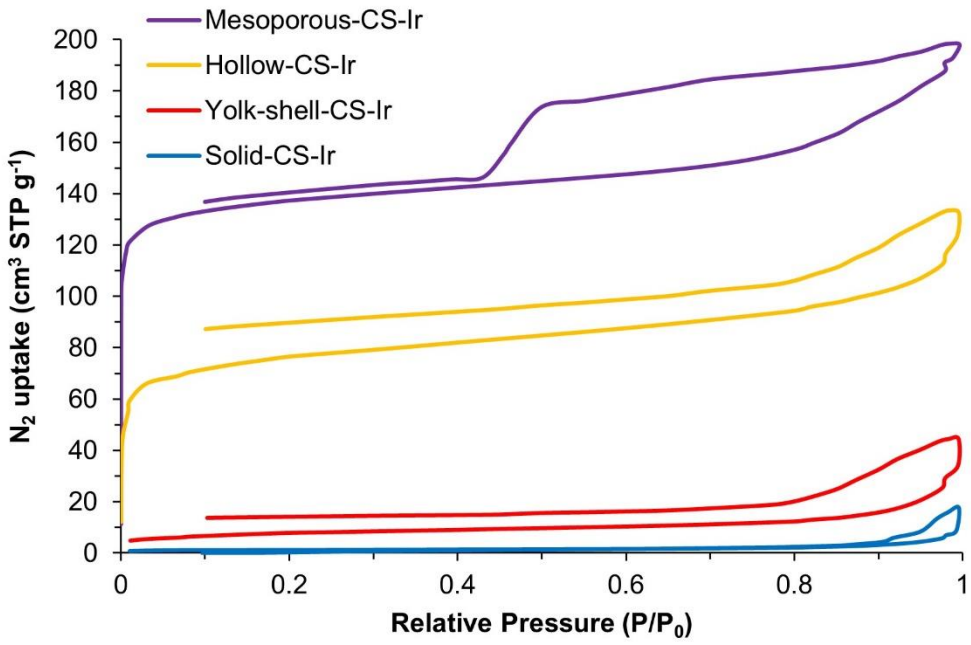

Figure 4. Comparison of nitrogen adsorption-desorption isotherms for the samples studied.

Furthermore, the ICP-MS demonstrated a similar trend for the exposed metal content of each sample which was expected as a higher specific surface-area should theoretically expose more Ir atoms (Table S2). The exposed Ir content measured with ICP-MS for Solid-CS-Ir, Yolk-shell-CS-Ir, Mesoporous-CS-Ir, and Hollow-CS-Ir, and was 0.08, 0.11, 1.82, and 0.26 wt.%, respectively. Unlike other synthetic methods that use strong acids to dissolve the template, which consequently removes a significant portion of SACs, ethanol was specifically chosen as the etchant since the interior oligomers are soluble in ethanol whereas Ir-EDTA is not. Thus, there is no concern of removing SACs during the dissolution process, leading to high Ir contents up to 1.82 wt.% for the exposed surface atoms.

In order to evaluate the chemical composition, Raman spectroscopy, XPS, and XAS studies were performed. Raman spectroscopy was used to evaluate the degree of graphitization (Figure S4). All of the samples displayed two peaks, a D band peak at 1340 cm^{-1} and a G band peak at 1600 cm^{-1}. The ratio between these two peaks (I_D/I_G) corresponds to the degree of graphitization, which was 1.10, 0.67, 0.62, and 0.61 for Solid-CS-Ir, Yolk-shell-CS-Ir, Mesoporous-CS-Ir, and Hollow-CS-Ir, respectively. Compared to the solid control sample, all of the samples that

underwent ethanol etching revealed significantly higher graphitization, indicating that the removal of short chain oligomers increases the graphitic domains during pyrolysis. This is in agreement with recent work that determined high molecular-weight polymers generate graphitic domains, whereas low molecular-weight polymers produce amorphous carbon.[20] In any case, graphitic domains are instrumental in increasing conductivity during electrocatalysis, thus further indicating the advantages of using the current method to prepare electrocatalysts.

To further investigate the chemical composition, XPS was used to evaluate the iridium, carbon, nitrogen, and oxygen species (Figure 5). The Ir 4f spectrum was deconvoluted into Ir $4f_{7/2}$ (61.18 eV) and Ir $4f_{5/2}$ (64.48 eV) peaks, suggesting an oxidation state slightly less than +4.[21] The C 1s spectrum was deconvoluted into five peaks: C=C (283.98 eV), C–C (284.58 eV), sp^2 C–N/O (285.18 eV), sp^3 C–N/O (285.98 eV), and C=O (287.98 eV).[10,13,22-25] A broad π–π* shake-up peak (291.98 eV) was present, confirming the existence of graphitic carbons.[26] The N 1s spectrum was deconvoluted into four peaks: pyridinic-N (397.88 eV), pyrrolic/Ir–N (399.48 eV), graphitic-N (400.68 eV), and oxidized-N (402.78 eV).[10,11,13,27,28] The O 1s spectrum was deconvoluted into four peaks: Ir–O (530.58 eV), C=O (532.08), C–O (532.98), and N=O (534.88 eV).[25,29] Lastly, the oxidation state and coordination environment were evaluated using XAS. The Iridium L-edge X-ray absorption near edge structure (XANES) spectrum in Figure S5A revealed the oxidation of iridium was +3.2 ± 0.9 , which is consistent with the XPS data. The coordination environment evaluated by extended X-ray absorption fine structure (EXAFS) indicated an average bond length of 1.90 Å, corresponding to Ir-N and Ir-O moieties (Figure S5B). Moreover, the absence of any Ir-Ir peaks confirms the iridium species is truly atomically dispersed. The R space data was also fitted to acquire structural parameters (Figure S5B and Table S4). Based on the fitting data, the coordination number (CN) of Ir SACs was determined to be 5.2 ± 1.1.

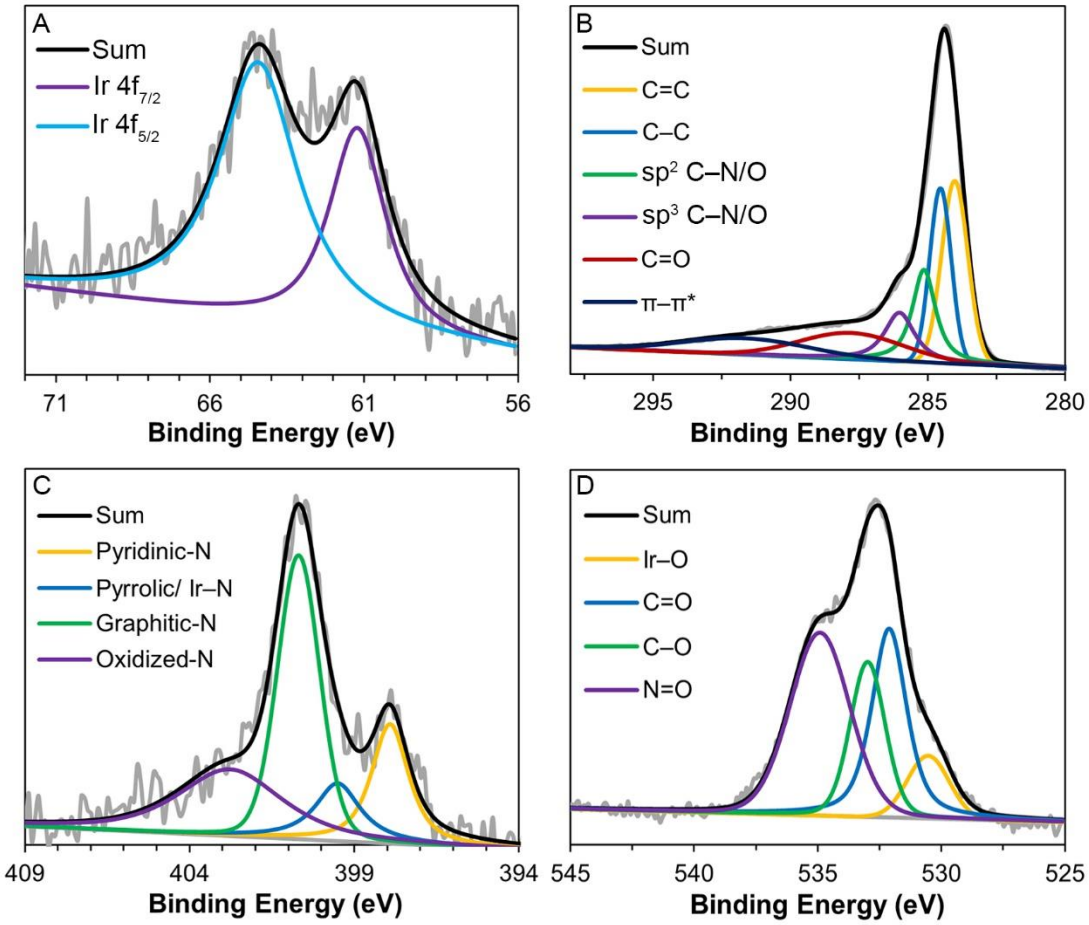

Figure 5. High-resolution XPS spectra of Mesoporous-CS-Ir. (A) Ir 4f, (B) C 1s, (C) N 1s, and (D) O 1s.

In an effort to demonstrate the catalytic performance and provide better incite of the structure-activity correlation between the various SACs, we investigated the samples toward formic acid oxidation (FAO) in an argon-saturated solution containing 0.5 M HCOOH and 0.5 M $HClO_4$. As evident by the FAO polarization curves in Figure 6, the activity decreases in the order of Mesoporous-CS-Ir, Hollow-CS-Ir, Yolk-shell-CS-Ir-E, and Solid-CS-Ir-E, which agrees well with the trends in both surface area and metal content. Impressively, all of the samples prepared in this work showed an FAO current density higher than that of 20 wt.% Ir/C. The peak current density for all samples also positively shifted compared to the Ir/C reference, indicative of a selectivity shift from an indirect pathway to a more favorable direct pathway. In the case of Ir nanoparticles, formic acid prefers to bridge between two neighboring Ir atoms and thus favors an indirect two-step reaction, where formic acid is first dehydrated into adsorbed CO (CO_{Ad}) and then

oxidized into CO_2.[30] Since CO_{Ad} binds very strongly to the Ir surface, it acts as a poisoning species by preventing any further catalysis. The Ir SACs on the other hand, do not have neighboring Ir atoms for formic acid to bridge to, and thus only single-site adsorption is possible, favoring a direct pathway, where formic acid undergoes sequential dehydrogenation to produce CO_2.[31] Other than the selectivity enhancement, the current density of Ir SACs is far superior to their nanoparticle counterparts. The max current density recorded for Mesoporous-CS-Ir was 30.6 mA cm^{-2}, which is one of the highest current densities reported for Ir SACs toward FAO. Table S5 shows a summary of the current density and corresponding mass activity of each sample. Clearly, we have demonstrated here that the SAC exposure directly correlates to a higher FAO activity; however, the coordination environment also plays a major role. It was recently revealed that Ir SACs are most active when asymmetrically coordinated to nitrogen and oxygen in an IrN_3O fashion.[32] Though our XPS and XAS studies suggest Ir binds to nitrogen and oxygen, the Fourier-transform EXAFS studies cannot normally quantify the N:O ratios due to their similar atomic weights.[33] However, the unprecedented FAO activity does suggest that the Ir SACs may exist in a similar IrN_xO_{5-x} geometry. In any case, the FAO activity can be optimized by simply modifying the synthetic conditions to favor a mesoporous structure and a high surface area.

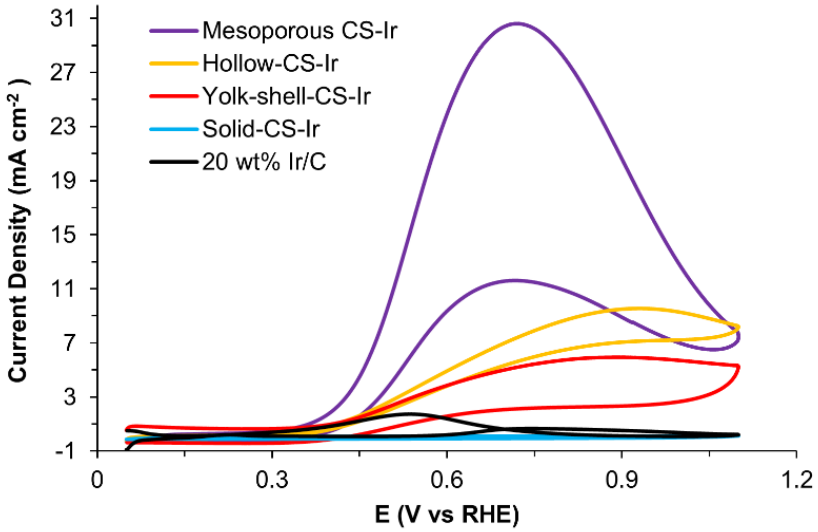

Figure 6. FAO polarization curves recorded in Ar-saturated 0.5 M HCOOH and 0.5 M $HClO_4$. All ORR polarization curves have been *iR* and background corrected.

Conclusions

In summary, we have successfully prepared a series of Ir-SAC-decorated carbon nanospheres using a kinetically-controlled growth strategy. The synthesis employs a chemical confinement strategy, with EDTA serving as a molecular barrier to spatially isolate Ir atoms in the polymer and then carbon matrix. Simultaneously, the porous structure of the carbon nanospheres can be readily adjusted through a kinetically-controlled polymerization process, where some of the interior region of the polymer nanospheres can be selectively dissolved with ethanol to produce yolk-shell, mesoporous, and hollow structures. The impact of the porous structure on FAO activity was also investigated. Owing to the high specific surface area and corresponding exposed metal content, Mesoporous-CS-Ir was demonstrated to be highly active toward FAO, with a peak current density of 30.6 mA cm^{-2}. Altogether, this work provides a one-pot, surfactant-free, and cost-effective synthesis of porous carbon nanospheres loaded with Ir-SACs at a level as high as 1.8 wt.%. The synthetic protocol should be extendible to other noble metals for the preparation of SACs for different catalytic reactions.

Experimental Section

Chemicals and materials. 3-Aminophenol, formaldehyde (37 wt.%), ammonium hydroxide (28–30 wt.%), sodium hexachloroiridate(III) hydrate, disodium ethylenediaminetetraacetate dihydrate, perchloric acid (70%), formic acid (95%), and Nafion (5 wt.%) were all purchased from Sigma-Aldrich. Ethanol (200 proof) was obtained from VWR. Aqueous solutions were prepared using deionized (DI) water with a resistivity of 18.2 MΩ·cm at room temperature.

Synthesis of Iridium-EDTA (Ir-EDTA) complex. Ir-EDTA was synthesized by following a published protocol with slight modifications.[34] Specifically, 0.092 g (0.273 mmol) of Na_2EDTA was dissolved in 2.0 mL of water and heated at 100 °C until dissolved. Next, 0.065 g (0.136 mmol) of Na_3IrCl_6 was dissolved in 1.0 mL of water and then added into the EDTA solution. The solution was heated to 150 °C for 24 h and filtered. The filtrate was freeze-dried with liquid N_2 to produce fine yellow powders of Ir-EDTA.

Synthesis of solid carbon nanospheres with Ir-SACs (Solid-CS-Ir). In a typical synthesis (see Table S1 for details), 0.6 g of 3-aminophenol was dissolved in a solution containing 44 mL of water and 12 mL of ethanol. Then, 0.15 g of the Ir-EDTA complex was added and dissolved,

followed by the addition of 0.2 mL of ammonium hydroxide. Finally, 0.36 mL of formaldehyde was added in one shot and the mixture was stirred at room temperature for 25 min. The polymer nanospheres were collected by centrifugation at 11,000 rpm for 15 min, followed by carbonization.

Synthesis of yolk-shell carbon nanospheres with Ir-SACs (Yolk-shell-CS-Ir). In a typical synthesis (see Table S1 for details), 0.6 g of 3-aminophenol was dissolved in a solution containing 44 mL of water and 12 mL of ethanol. Then, 0.15 g of the Ir-EDTA complex was added, followed by the addition of 0.2 mL of ammonium hydroxide. Next, 0.36 mL of formaldehyde was added in one shot and the mixture was stirred for 25 min at room temperature. The solid product was collected by centrifugation at 11,000 rpm for 10 min and then redispersed in 40 mL of ethanol under mild sonication for 30 min to partially dissolve some of the interior region. The resulting yolk-shell polymer nanospheres were collected by centrifugation at 10,000 rpm for 10 min, followed by carbonization.

Synthesis of mesoporous carbon nanospheres with Ir-SACs (Mesoporous-CS-Ir). In a typical synthesis (see Table S1 for details), 0.2 g of 3-aminophenol was dissolved in a solution containing 44 mL of water and 12 mL of ethanol. Then, 0.15 g of the Ir-EDTA complex was added, followed by the addition of 0.2 mL of ammonium hydroxide. Next, 0.12 mL of formaldehyde was added at a rate of 1 drop (0.026 mL) per minute and the mixture was stirred at room temperature for 25 min. The solid product was collected by centrifugation at 11,000 rpm for 10 min and then redispersed in 40 mL of ethanol for 30 min to partially dissolve some of the interior region. The resulting mesoporous polymer nanospheres were collected by centrifugation at 10,000 rpm for 10 min, followed by carbonization.

Synthesis of hollow carbon nanospheres with Ir-SACs (Hollow-CS-Ir). In a typical synthesis (see Table S1 for details), 0.6 g of 3-aminophenol was dissolved in a solution containing 56 mL of water. Then, 0.15 g of the Ir-EDTA complex was added and dissolved, followed by the addition of 0.05 mL of ammonium hydroxide. Next, 0.36 mL of formaldehyde was added dropwise at a rate of 1 drop (0.026 mL) every 20 s and the mixture was stirred for 25 min at room temperature. The solid product was collected by centrifugation at 11,000 rpm for 10 min and then redispersed in 40 mL of ethanol under mild sonication for 30 min to dissolve the interior region. The resulting hollow polymer nanospheres were collected by centrifugation at 10,000 rpm for 10 min, followed by carbonization.

Carbonization and in-situ reduction. The carbon nanospheres containing Ir-SACs were

prepared by heating the polymer nanospheres in a tube furnace under N_2 flow up to a final temperature of 925 °C at a heating rate of 5 °C min^{-1} for 3 h.

Characterizations. High-angle annular dark-field scanning TEM (HAADF-STEM) and energy dispersive X-ray (EDX) mapping images were acquired using an aberration-corrected Hitachi HD-2700 STEM. Prior to TEM analysis, the sample was dispersed in ethanol by moderate sonication, followed by deposition on a lacey carbon-coated, 200-mesh, copper TEM grid by drop-casting, followed by drying under ambient conditions. Scanning electron microscopy (SEM) images were obtained using a Hitachi SU-8230 microscope. Prior to SEM analysis, samples were dispersed in ethanol by moderate sonication and then deposited on silicon wafers and dried under ambient conditions. Nitrogen adsorption measurement was performed using an auto-adsorption analyzer (micromeritics, 3Flex) at –196 °C. The Ir content was measured using a PerkinElmer NexION 300Q inductively-coupled plasma mass spectrometer (ICP-MS). The sample was prepared by leaching out the Ir atoms in a 3:1 mixture of hydrochloric acid and nitric acid. The Raman spectra were collected using a Renishaw inVia Raman Spectrometer integrated with a Leica microscope. X-ray photoelectron spectroscopy (XPS) data was collected on a Thermo K-Alpha spectrometer with an Al Kα source. X-ray absorption spectroscopy (XAS) experiments on Ir L-edge were conducted in fluorescence mode at beamline 9-BM of the Advanced Photon Source (APS) at Argonne National Laboratory. The data obtained from XAS were processed and analyzed using the ATHENA program.[35] The average valence state of Ir SACs was interpolated from the first derivative maximum (K-edge absorption threshold) of the sample compared to that of Ir metal and IrO_2 references. The least-squares EXAFS fitting data was configured from the coordination route of known metal nitride and oxide references using the ARTEMIS program.[35]

Catalytic measurements. The electrochemical measurements were conducted at room temperature using a three-electrode cell and a CHI 600E potentiostat electrochemical workstation. A glassy carbon rotating disk electrode (RDE, 5 mm in diameter) loaded with the catalyst served as the working electrode, together with a Pt wire in a fritted isolation tube as the counter electrode and reversible hydrogen electrode (RHE) as the reference electrode. The working electrode was prepared by polishing with 0.3-μm Al_2O_3 slurry and washing with water and ethanol. The working electrode was then polished in the same fashion using 0.05-μm Al_2O_3 slurry. The catalyst ink was prepared by ultrasonicating 10 mg of the SAC catalyst with a mixture containing 312.5 μL of H_2O, 937.5 μL of ethanol, and 20 μL of 5 wt.% Nafion solution for 1 h to form a homogeneous

suspension. Afterwards, 9 μL of the as-prepared catalyst ink was dropped on the polished RDE and dried at room temperature. As a benchmark, Ir/C catalyst ink (20 wt.% Ir nanoparticles on Vulcan XC-72 carbon support, Premetek Co.) was prepared using the same protocol. Before electrochemical measurements, all solutions were purged and saturated with Ar. To measure FAO activity, the catalyst was first cycled 30 times between 0.05–1.1 V_{RHE} at 100 mV s^{-1} in Ar-saturated 0.1 M $HClO_4$. A background CV was obtained under the same conditions except the scan rate was reduced to 10 mV s^{-1}. FAO measurements were conducted by cycling the potential 10 times between 0.1–1.1 V_{RHE} at 10 mV s^{-1} in an Ar-saturated solution containing 0.5 M $HClO_4$ and 0.5 M HCOOH at 1,600 rpm. The FAO plots were corrected for double-layer capacitance by subtracting the background CV scan. All of the electrochemical data was *iR*-compensated at 85%.

Acknowledgements

This work was supported in part by the Department of Energy, Office of Basic Energy Sciences, Catalysis Science Program (grant DE-FG02-05ER15731) and start-up funds from the Georgia Tech. Part of the electron microscopy characterization work was performed at the Georgia Tech Institute for Electronics and Nanotechnology, a member of the National Nanotechnology Coordinated Infrastructure (NNCI), which is supported by the National Science Foundation (ECCS-2025462). This research also used resources of the Advanced Photon Source, a U.S. Department of Energy (DOE) Office of Science user facility operated for the DOE Office of Science by Argonne National Laboratory under Contract No. DE-AC02-06CH11357. The authors would like to thank Debora Motta Meira for providing the Ir L-edge spectra of Ir standards.

Data availability Statement

The data that support the findings of this study are available in the supplementary material of this article.

References

[1] M. Wang, Y. Hu, J. Pu, Y. Zi, W. Huang, *Adv. Mater.* **2023**, 2303492.

[2] H. Zhang, X. F. Lu, Z. P. Wu, X. W. D. Lou, *ACS Cent. Sci.* **2020**, *6*, 1288-1301.

[3] Q. Zhang, J. Guan, *Adv. Funct. Mater.* **2020**, *30*, 2000768.

[4] L. Li, X. Chang, X. Lin, Z. J. Zhao, J. Gong, *Chem. Soc. Rev.* **2020**, *49*, 8156-8178.

[5] Y. Zhang, J. Yang, R. Ge, J. Zhang, J. M. Cairney, Y. Li, M. Zhu, S. Li, W Li, *Coord. Chem. Rev.* **2022**, *461*, 214493.

[6] H. Yang, L. Shang, Q. Zhang, R. Shi, G. I. Waterhouse, L. Gu, T. Zhang, *Nat. commun.* **2019**, *10*, 4585.

[7] C. M. Wang, Y. D. Wang, J. W. Ge, Z. K. Xie, *Chem* **2019**, *5*, 2736-2737.

[8] J. Xi, S. Yang, L. Silvioli, S. Cao, P. Liu, Q. Chen, Y. Zhao, H. Sun, J. N. Hansen, J. P. B. Haraldsted, *J. Catal.* **2021**, *393*, 313-323.

[9] C. Rivera-Cárcamo, P. Serp, *ChemCatChem* **2018**, *10*, 5058-5091.

[10] J. Jeskey, Y. Ding, Y. Chen, Z. D. Hood, G. E. Sterbinsky, M. Jaroniec, Y. Xia, *JACS Au* **2023,** *3*, 3227-3236.

[11] X. Li, Y. Song, L. You, L. Gao, Y. Liu, W. Chen, L. Mao, *Ind. Eng. Chem. Res.* **2019**, *58*, 2933-2944.

[12] Z. Lei, N. Christov, L. L. Zhang, X. S. Zhao, *J. Mater. Chem.* **2011**, *21*, 2274-2281.

[13] J. Jeskey, Y. Chen, S. Kim, Y. Xia, *Chem. Mater*. **2023**, 35, 3024-3032.

[14] D. S. Bin, Z. X. Chi, Y. Li, K. Zhang, X. Yang, Y. G. Sun, J. Y. Piao, A. M. Cao, L. J. Wan, *J. Am. Chem. Soc.* **2017**, *139*, 13492-13498.

[15] J. Du, Y. Zhang, H. Wu, S. Hou, A. Chen, *Carbon* **2020**, *156*, 523-528.

[16] J. Tao, J. Zhou, Z. Yao, Z. Jiao, B. Wei, R. Tan, Z. Li, *Carbon* **2021**, *172*, 542-555.

[17] R. Yu, X. Huang, Y. Liu, Y. Kong, Z. Gu, Y. Yang, Y. Wang, W. Ban, H. Song, C. Yu, *Adv. Sci.* **2020**, *7*, 2000393.

[18] K. Liang, C. Yuan, X. Zhou, Z. Yang, J. Du, Y. Ye, J. Luo, C. Chen, J. Zhu, C. Su, *J. Mater. Chem. A* **2021**, *9*, 13908-13915.

[19] J. Qiu, Z. Chen, M. Chi, Y. Xia, *Angew. Chem. Int. Ed.* **2021**, *60*, 12980-12984.

[20] J. Bai, S. Wang, Y. Li, Z. Wang, J. Tang, *Int. J. Bio. Macromol.* **2021**, *187*, 594-602.

[21] S. J. Freakley, J. Ruiz-Esquius, D. J. Morgan, *Surf. Interface Anal.* **2017**, *49*, 794-799.

[22] B. J. Matsoso, K. Ranganathan, B. K. Mutuma, T. Lerotholi, G. Jones, N. J. Coville, *RSC Adv.* **2016**, *6*, 106914-106920.

[23] B. Yu, X. Wang, X. Qian, W. Xing, H. Yang, L. Ma, Y. Lin, S. Jiang, L. Song, Y. Hu, *RSC Adv.* **2014**, *4*, 31782-31794.

[24] H. Shen, J. Zhou, Y. Zhao, S. Zhang, X. Bi, S. Zhuo, H. Cui, *RSC Adv.* **2016**, *6*, 58764-58770.

[25] M. Ayiania, M. Smith, A. J. Hensley, L. Scudiero, J. S. McEwen, M. Garcia-Perez, *Carbon* **2020**, *162*, 528-544.

[26] T. R. Gengenbach, G. H. Major, M. R. Linford, C. D. Easton, *J. Vac. Sci. Technol. A: Vac. Surf. Films* **2021**, *39*, 013204.

[27] N. B. Magaela, R. Matshitse, B. Babu, M. Managa, E. Prinsloo, T. Nyokong, *Polyhedron* **2022**, *213*, 115624.

[28] L. Yi, B. Feng, N. Chen, W. Li, J. Li, C. Fang, Y. Yao, W. Hu, *Chem. Eng. J.* **2021**, *415*, 129034.

[29] R. Martin, M. Kim, C. Lee, V. Mehar, S. Albertin, U. Hejral, L. R. Merte, E. Lundgren, A. Asthagiri, J. Weaver, *J. Phys. Chem. Lett.* **2020**, *11*, 7184-7189.

[30] J. Xu, D. Yuan, F. Yang, D. Mei, Z. Zhang, Y. X. Chen, *Phys. Chem. Chem. Phys.* **2013**, *15*, 4367-4376.

[31] Z. Li, Y. Chen, S. Ji, Y. Tang, W. Chen, A. Li, J. Zhao, Y. Xiong, Y. Wu, Y. Gong, *Nat. Chem.* **2020**, *12*, 764-772.

[32] L. Wang, B. Ji, Y. Zheng, Y. Tang, *Angew. Chem. Int. Ed.* **2023**, *62*, e202301711.

[33] W. Zhang, Q. Fu, Q. Luo, L. Sheng, J. Yang, *JACS Au* **2021**, *1*, 2130-2145.

[34] M. Saito, T. Uehiro, Y. Yoshino, *Bull. Chem. Soc. Jpn.* **1980**, *53*, 3531-3536.

[35] B. Ravel, M. Newville, *J. Synchrotron Radiat.* **2005**, *12*, 537-541.

For Table of Contents Only

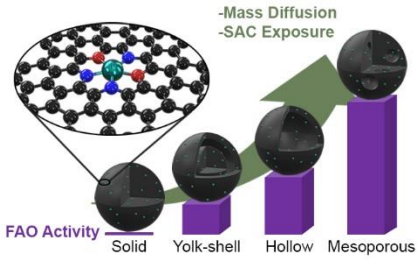

Table of Contents Text: **Iridium single-atoms loaded on carbon nanospheres with varying architectures:** solid, yolk-shell, hollow, and mesoporous carbon nanospheres loaded with Ir SACs have been prepared using a simple, one-pot synthesis. Benefiting from the improved active site exposure and mass diffusion, these catalysts exhibit high activities toward formic acid oxidation.